energies

MDPI

Article

Vertical-Axis Tidal Turbines: Model Development and Farm Layout Design

Micol Pucci *, Raffaele Spina and Stefania Zanforlin *

Department of Energy, Systems, Territory and Constructions Engineering, University of Pisa, Largo Lucio Lazzarino, 56122 Pisa, Italy

* Correspondence: micol.pucci@phd.unipi.it (M.P.); stefania.zanforlin@unipi.it (S.Z.)

Abstract: In this paper, we propose a new 3D model for vertical-axis tidal turbines (VATTs) embedded in the shallow-water code SHYFEM. The turbine model is based on the Blade-Element\Momentum (BEM) theory and, therefore, is able to predict turbine performance based on the local flow conditions and the geometric characteristics of the turbine. It is particularly suitable for studying turbine arrays, as it can capture the interactions between the turbines. For this reason, the model is used to test a tidal farm of 21 devices with fluid dynamic simulations. In particular, we deploy the farm at Portland Bill, which is a marine site characterised by a wide spread in the direction of the tidal currents during a flood-ebb tide cycle. We optimised the lateral and longitudinal spacing of the turbines in a fence using computational fluid dynamics simulations and then performed a sensitivity analysis by changing the distance between the fences. The results show that the greater the distance between the fences, the higher the power output. The increase in power generation is around 16%, but this implies a huge increase in the horizontal extent of the farm. Further assessments should be carried out, as the expansion of a marine area dedicated to energy exploitation may conflict with other stakeholder interests.

Keywords: vertical-axis tidal turbine; BEM; shallow-water equations; farm design

Citation: Pucci, M.; Spina, R.; Zanforlin, S. Vertical-Axis Tidal Turbines: Model Development and Farm Layout Design. *Energies* **2024**, *17*, 2366. https://doi.org/10.3390/en17102366

Academic Editors: Jérôme Thiebot, Eric L. Bibeau and Sylvain Guillou

Received: 21 March 2024
Revised: 6 May 2024
Accepted: 11 May 2024
Published: 14 May 2024

1. Introduction

Tidal energy is gaining popularity as a viable renewable energy resource, capable of diversifying a country's energy mix. Horizontal-axis tidal turbines (HATTs) are the most commonly used devices for exploiting tidal currents. However, vertical-axis tidal turbines (VATTs) have also reached a comparable Technology Readiness Level (TRL). Since experimental campaigns are costly and prohibitive, there is a need for tools to test full-scale devices in a realistic environment. Such a tool should be able to reproduce turbine behaviour in terms of power and wake development, and capture interactions between devices in a cluster. Additionally, it should be able to evaluate the behaviour of a cluster or farm located in a specific marine site. To achieve this, it is recommended to use a regional code in combination with a specific turbine model. The literature contains several examples of regional codes used for energy evaluation purposes. We can distinguish between two-dimensional and three-dimensional cases: two-dimensional cases adopt a turbine parametrization consisting of increasing the bed friction at the turbine sites, while three-dimensional cases use a momentum sink approach. Some examples of the first approach can be found in [1], where a bed friction model of the turbine was adopted to simulate 12 devices, or in [2], where up to 266 devices were simulated. As the number of devices increases, the turbines become a sub-grid element (i.e., more than one turbine is deployed in a grid element), such as in [3], where more than 8000 devices were analysed.

Two-dimensional analyses are useful for general and preliminary assessments, but they cannot provide reliable results for resource and environmental impact studies. In [4], there was a comparison between a 2D and a 3D analysis, which showed how a 3D model

can reproduce the bypass flow around a turbine, contributing to reducing the velocity in the rotor region by about 20–25% compared to a 2D evaluation and resulting in less optimistic power generation assessments. Moreover, the velocity at the seabed is 10% higher in the 3D case (due to the bypass flow). Therefore, the environmental impact in terms of seabed erosion cannot be assessed with 2D models. Indeed, the use of 2D models in the presence of energy converters results in a lower flow velocity averaged through the water column in correspondence with the devices. A lower flow velocity results in less seabed erosion, as shown in [5]. However, this is not a representation of a realistic situation, as the presence of energy devices causes the flow to accelerate at the seabed, enhancing seabed erosion.

All these considerations point to the need for 3D studies. Some examples of 3D momentum sink analysis can be found in [6–8] using the regional solvers FVCOM, ROMS, and Delft3DFlow, respectively. In these studies, a large number of turbines were simulated and the turbine was a sub-grid element. In [9], an example of a single device analysis was presented, where the turbine occupied a single grid element. In [10], a more detailed study was presented, where the turbine was represented by several grid elements. Additionally, in [11], the turbine was also represented by several grid elements, with the peculiarity that in addition to the momentum sink terms, it used turbulence source terms injected at the rotor disc location. The 3D momentum sink method is often adopted in the literature (and in all the 3D works mentioned above) using an actuator disc approach. Thus, the behaviour of the turbine is predetermined by imposing a thrust coefficient. To the best of the authors' knowledge, there are only two examples (using a regional code) of turbine models that use the momentum sink approach coupled with a Blade-Element\Momentum (BEM) model to represent the turbines. The first example is that developed in [12] in the Delft3DFlow code. The second is the model developed for the regional code SHYFEM, as described in [13]. The application of a BEM-based model allows for the prediction of turbine behaviour in terms of power output and wake development, i.e., the flow field surrounding the turbine, based on the local flow conditions (occurring at the considered blade element) and the geometric design of the specific turbine under consideration. The performance of a turbine in a cluster or farm is, therefore, determined by the surrounding flow field, i.e., the mutual influence between the devices is taken into consideration. It is worth noting that all the studies in the literature focus solely on HATTs. To the best of the authors' knowledge, there are no examples in the literature of studies on VATTs in a regional code. Therefore, the purpose of this paper is to introduce a VATT model in a regional code. In particular, we use the SHYFEM code [14] and develop the VATT model similarly to what was done in [13] for HATTs.

The simulation of VATTs is particularly challenging due to unsteady effects such as dynamic stalls. High-fidelity blade-resolved CFD should be used to effectively capture these phenomena, but it is highly demanding due to the spatial and temporal resolution required, as shown in [15]. It is prohibitive to use CFD blade-resolved for turbine arrays: small clusters of three or four turbines are usually simulated only in two-dimensional domains, as in [16,17] or in [18]. There are some computationally efficient turbine parametrizations based on the Actuator Line Model (ALM), as in [19], but they are still highly demanding to perform arrays, as stated in [20]. Indeed, some examples of cluster analyses are performed in 2D even with simplified turbine models. For example, in [21], the Actuator Cylinder (AC) was adopted to simulate four platforms, each one made up of four turbines, using the Hydroquest turbine.

Due to the above-mentioned problems, the study of tidal turbines cannot be limited to 2D analysis. Therefore, there is a need for a tool capable of reproducing VATT clusters/farms in three-dimensional domains and in realistic conditions. Our aim is to develop a tool that could be used to simulate VATT farms with relatively low computational time but with a certain level of accuracy. We believe that a plausible solution is to adopt the simplicity of a regional code with a BEM-based turbine model. For this reason, in this paper, we present the development of a VATT model within the SHYFEM code.

In Section 2, we analyse the model development, which is validated against experimental data in Section 3. Section 4 describes the sensitivity analysis carried out. Section 5

describes the ability of the model to capture interactions between devices by analysing a pair of turbines. In Section 6, we focus on a tidal farm, where the spacing between turbines in a fence has been optimised, and then we perform a sensitivity analysis of the spacing between the fences. The results are analysed in Section 7, and we draw some conclusions in Section 8.

2. Model Development

This section describes the VATT model embedded within the SHYFEM code. SHYFEM is an open-access code developed at the National Research Council-Institute of Marine Sciences (CNR-ISMAR) of Venice. The program uses a finite element for the horizontal discretisation of the domain, while the vertical water column is discretized into N_l layers of thickness h_l. The hydrodynamic core of the code in the most general formulation is now briefly summarised. It adopts the shallow-water assumption for three-dimensional analyses using a hydrostatic approach. The equations of motion integrated on each vertical layer l are:

$$\frac{\delta U_l}{\delta t} + Adv_l^x - fV_l + gh_l\frac{\delta \zeta}{\delta x} + S_X = -\frac{gh_l}{\rho_0}\int_{-H_l}^{\zeta}\rho' dz + \\ -\frac{h_l}{\rho_0}\frac{\delta p_a}{\delta x} + A_H\left(\frac{\delta^2 U_l}{\delta x^2} + \frac{\delta^2 U_l}{\delta y^2}\right) + \frac{(\tau_x^{top(l)} - \tau_x^{bottom(l)})}{\rho_0} \quad (1)$$

$$\frac{\delta V_l}{\delta t} + Adv_l^y - fU_l + gh_l\frac{\delta \zeta}{\delta y} + S_Y = -\frac{gh_l}{\rho_0}\int_{-H_l}^{\zeta}\rho' dz + \\ -\frac{h_l}{\rho_0}\frac{\delta p_a}{\delta y} + A_H\left(\frac{\delta^2 V_l}{\delta x^2} + \frac{\delta^2 V_l}{\delta y^2}\right) + \frac{(\tau_y^{top(l)} - \tau_y^{bottom(l)})}{\rho_0} \quad (2)$$

where U_l and V_l are the horizontal velocities in the x and y directions, respectively, integrated over layer l as $U_l = \int_{H_l}^{H_{l-1}} u_l dz$ and $V_l = \int_{H_l}^{H_{l-1}} v_l dz$; u_l and v_l are the horizontal velocities not integrated; H_l is the depth of the bottom of layer l; p_a is the atmospheric pressure; f is the Coriolis parameter; g is the gravity acceleration; ζ is the free surface level; ρ_0 is the constant water density; ρ' is the variable density such that $\rho = \rho_0 + \rho'$; h_l is the layer thickness; and A_H is the horizontal eddy viscosity. $S_{X\backslash Y}$ are other external factors, such as momentum sinks for turbine representations. The other terms of the equation are defined as follows:

$$Adv_l^x = u_l\frac{\delta U_l}{\delta x} + v_l\frac{\delta U_l}{\delta y} + \int_{z_l}^{z_{l-1}} w\frac{\delta u}{\delta z}dz \quad (3)$$

$$Adv_l^y = u_l\frac{\delta V_l}{\delta x} + v_l\frac{\delta V_l}{\delta y} + \int_{z_l}^{z_{l-1}} w\frac{\delta v}{\delta z}dz \quad (4)$$

$$\tau_x^{top(l)} = \rho_0 A_V\frac{\delta u_{l-1}}{\delta z} \quad (5)$$

$$\tau_y^{top(l)} = \rho_0 A_V\frac{\delta v_{l-1}}{\delta z} \quad (6)$$

$$\tau_x^{bottom(l)} = \rho_0 A_V\frac{\delta u_l}{\delta z} \quad (7)$$

$$\tau_y^{bottom(l)} = \rho_0 A_V\frac{\delta v_l}{\delta z} \quad (8)$$

where A_V is the vertical eddy viscosity. The continuity equation integrated over each vertical layer is:

$$\frac{\delta U_l}{\delta x} + \frac{\delta V_l}{\delta y} = w_l - w_{l-1} \quad (9)$$

where w is the vertical velocity. The integration of the continuity equation vertically along the water column provides the equation for the free surface level:

$$\frac{\delta \zeta}{\delta t} + \sum_l \frac{\delta U_l}{\delta x} + \sum_l \frac{\delta V_l}{\delta y} = 0 \tag{10}$$

In order to represent the turbine within the SHYFEM code, we introduce the momentum sink terms in Equations (1) and (2). In particular, we act on the S_X and S_Y terms. To calculate the latter terms, we need to evaluate the forces acting on a blade element and then apply equal and opposite forces to the flow. Referring to Figure 1, the force coefficients can be calculated as follows:

$$C_n = C_L \cos\alpha + C_D \sin\alpha \tag{11}$$
$$C_t = C_L \sin\alpha - C_D \cos\alpha \tag{12}$$
$$C_x = C_n \sin\theta - C_t \cos\theta \tag{13}$$
$$C_y = (-C_n \cos\theta - C_t \sin\theta) \cdot sign_{rot} \tag{14}$$

where θ is the azimuth position; $sign_{rot}$ is the direction of rotation (+1 counterclockwise; -1 clockwise); C_n and C_t are the coefficients of the normal and tangential forces, where the normal and tangential directions are the radial and tangential directions in Figure 1; and C_x and C_y are the coefficients of the x and y forces. The latter forces are:

$$F_x = \frac{1}{2}\rho c W_{rel}^2 \cdot C_x \cdot dh \tag{15}$$
$$F_y = \frac{1}{2}\rho c W_{rel}^2 \cdot C_y \cdot dh \tag{16}$$

where dh is the vertical extent of the grid element to which the forces are applied. The relative velocity is $W_{rel} = \sqrt{W_n^2 + W_t^2}$, where the normal and tangential components are:

$$W_n = u \cdot \sin\theta - sign_{rot} \cdot v \cos\theta \tag{17}$$
$$W_t = u \cdot \cos\theta + sign_{rot} \cdot (v \sin\theta + \Omega \cdot R) \tag{18}$$

where Ω is the rotation speed and R is the turbine radius. In order to introduce the momentum sink terms, we must first consider the number of blades B and the fraction of the revolution time that each grid element is virtually occupied by the blade passage. To do this, consider the grid detail in the turbine area shown in Figure 2. If we consider a top view of the device, the grid representation of a vertical-axis turbine consists of a ring, namely the footprint of the blade revolution is a ring on a horizontal plane. Consider having on the turbine ring N_r elements of approximately equal azimuthal extent: each element will be occupied by the blade passage for $\frac{1}{N_r}$-th of the revolution time. Therefore, the final versions of the x and y forces are as follows:

$$F_x = \frac{1}{2}\rho c W_{rel}^2 \cdot C_x \cdot dh \cdot B \cdot \frac{1}{N_r} \tag{19}$$
$$F_y = \frac{1}{2}\rho c W_{rel}^2 \cdot C_y \cdot dh \cdot B \cdot \frac{1}{N_r} \tag{20}$$

and the momentum sink terms in Equations (1) and (2) are:

$$S_{X\backslash Y} = \frac{F_{x\backslash y}}{\rho A_{footprint}} \tag{21}$$

where $A_{footprint}$ is the horizontal area of the grid element, namely the footprint area. It should be noted that Equation (21) displays the x- and y-momentum sink terms. There

is no z-momentum sink because, as previously stated, the SHYFEM code utilises the hydrostatic assumption. This means that there is no z-momentum equation; therefore, z-momentum sink terms cannot be introduced. However, for a straight-blade turbine, there are no forces acting along the vertical direction of the blade. There would be a force along the vertical direction, but only in the case of a turbine with curved blades, with an approximate troposkein geometry. In such as case, the corresponding force coefficient would be $C_z = -C_n \sin \gamma_c$, where γ_c denotes the local curvature of the blade section with respect to a horizontal plane. However, in this study, we focused on the H-Darrieus turbine with straight blades, and therefore γ_c is 0 everywhere along the blade, so no z forces are present. Therefore, by omitting the z-momentum sink term, we commit no errors.

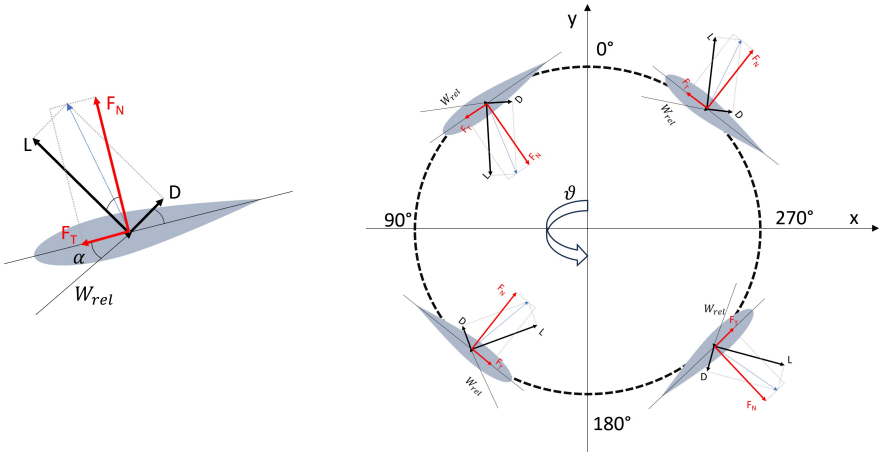

Figure 1. Schematic representation of a vertical-axis turbine at a generic horizontal plane, with a focus on the forces acting on a blade element.

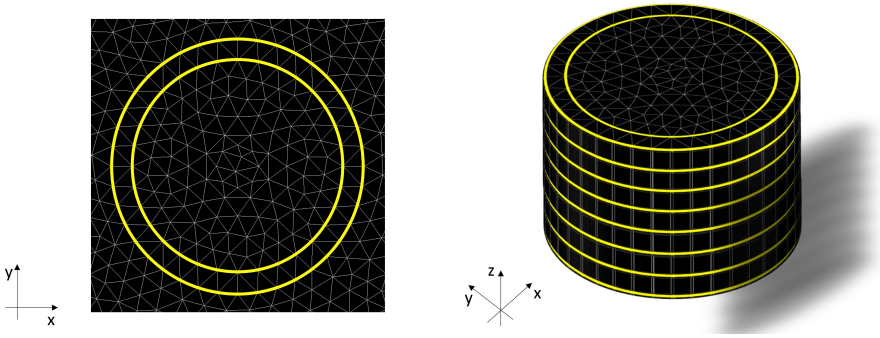

Figure 2. Detail of an SHYFEM mesh for a vertical-axis turbine. On the left is the top view of the turbine elements, namely the elements inside the yellow ring. On the right is a three-dimensional view of the turbine made up of several layers.

Sub-Models

The main phenomena to be considered in the analysis of vertical-axis turbines are dynamic stall and flow curvature effects. The former occurs as during the rotation of a blade, the angle of attack changes cyclically and significantly: the increase in the angle of attack leads to higher lift coefficient peaks compared to those reached in static conditions. This effect is due to the development of the so-called Leading-Edge Vortex (LEV) near the blade. This vortex increases the suction on the wing, preventing and delaying stall. To further increase the angle of attack, the LEV moves towards the trailing edge, causing the lift force to decrease. These processes are reproduced by embedding the dynamic stall model developed at the University of Pisa into the turbine model, as described in detail in [22].

The flow curvature effect was analysed in detail in [23]. To calculate the forces acting on a blade of a vertical-axis turbine, it is common practice to evaluate the relative velocity

W_{rel} and the angle of attack α at the point of attachment of the turbine blade to its support arm. However, as the radial distance from the turbine axis varies along the blade chord, so do the relative velocity and angle of attack. This effect becomes more relevant as the chord-to-radius ratio increases. Therefore, it is clear that an airfoil in a curvilinear flow has different aerodynamic characteristics compared to the same airfoil in a rectilinear flow. In particular, it is possible to change the geometry of the airfoil in the curvilinear flow, creating a virtual airfoil, in order to reproduce the same aerodynamic behaviour as in a rectilinear flow. A symmetrical airfoil in a curvilinear flow is aerodynamically equivalent to a virtual airfoil in a rectilinear flow, which is cambered and has a different effective angle of incidence α_i. So, the virtual airfoil is characterised by a virtual camber c_v and a virtual incidence α_i. Both of these values change as the azimuthal position changes, but usually, the average value is taken. Therefore, to correctly represent an airfoil in a curvilinear flow, the angle of attack α, used to calculate the force coefficients on the blades, as in Equations (11) and (12), should be:

$$\alpha = \alpha_i + c_v \tag{22}$$

$$\alpha_i = \left(\frac{c}{2} - x_n\right)\frac{|\Omega|}{W_{rel}} \tag{23}$$

$$c_v = \left(\frac{3c}{4} - x_n\right)\frac{|\Omega|}{W_{rel}} \tag{24}$$

where x_n is the hook point of the blade.

3. Validation

To validate the SHYFEM model for VATTs, we use the experimental campaign described in [24,25] relative to a two-bladed H-Darrieus wind turbine as a benchmark. Since our validation benchmark is a wind test, i.e., using air as the working fluid, while SHYFEM uses water, we have to consider the similarities. Geometric similarity is maintained because we reproduce the same turbine on a 1:1 scale. To achieve kinematic similarity, the velocity triangles in homologous sections should be geometrically similar. To this end, by equating the Reynolds numbers of the experimental situation and the SHYFEM simulation (subscripts E and S, respectively), we obtain:

$$Re_S = Re_E \tag{25}$$

$$\frac{\rho_S U_{\infty S} D_S}{\mu_S} = \frac{\rho_E U_{\infty E} D_E}{\mu_E} \tag{26}$$

$$\frac{U_{\infty S}}{U_{\infty E}} = \frac{\rho_E}{\rho_S}\frac{\mu_S}{\mu_E}\frac{D_E}{D_S} \tag{27}$$

where ρ_E is the air density (1.22 kg/m^3), μ_E is the air dynamic viscosity (1.81×10^{-5} Pa · s), ρ_S is the water density (998 kg/m^3), and μ_S is the water dynamic viscosity (1×10^{-3} Pa · s). The diameter ratio is equal to 1. Since the undisturbed flow velocity in the experimental conditions was set to 10.7 m/s, the resulting undisturbed velocity for the SHYFEM simulations is 0.72 m/s. At this point, it is sufficient to use the same Tip-Speed Ratio (TSR), i.e., 3, to ensure kinematic similarity. The TSR is defined as:

$$TSR = \frac{R\Omega}{U_\infty} \tag{28}$$

where U_∞ is the undisturbed flow velocity. As explained in [26], to achieve dynamic similarity, the lift and drag coefficients should be equal in homologous sections. These coefficients are a function of the Reynolds number and the angle of attack. Therefore, to achieve dynamic similarity, it is necessary to have the same Reynolds number and angle of attack in homologous sections of the blade. The Reynolds number is constrained to be the

same in both situations. We obtain the same chord-based Reynolds number, about 110,000, which is defined as

$$Re_c = \frac{\rho_S \cdot c \cdot TSR \cdot U_{\infty S}}{\mu_S} \tag{29}$$

As the TSR is the same in both situations, the speed triangles at different blade sections are similar, so the inflow angle is the same. As the twist angle is the same in both cases (i.e., 0), the resulting angles of attack are the same.

3.1. Performance Validation

For performance validation, we use several sets of experimental data relating to three different wind tunnels. Two of them are open-jet wind tunnels: the OJF at Delft University of Technology and the L1-A at the von Karman Institute for Fluid Dynamics (VKI). Both tunnels have a jet nozzle diameter of 3 m; the OJF is octagonal, while the L1-A is circular. The free jet section is 4.5 m long for the L1-A and up to 13 m long for the OJF. The turbulence intensity levels are around 0.3%. The other wind tunnel is at the Politecnico di Milano (GVPM). It is a closed-circuit wind tunnel arranged in a vertical layout with two test chambers in the loop. The test section is 13.84 m wide, 3.84 m high, and 35 m long. Due to the large domain for the experimental test at the GVPM, the SHYFEM domain extents are also large, as described in Table 1, along with the other setup conditions. The horizontal grid resolution in the turbine region is about 0.05 m and gradually increases towards the boundaries to 0.25 m. The vertical discretisation uses layers with a thickness of 0.05 m in the turbine region, gradually increasing up to 0.2 m.

Table 1. Model setup for validation.

Validation Setup	
x domain extension	40 m
y domain extension	10 m
z domain extension	10 m
Turbine chord (c)	0.05 m
Turbine diameter (D_t)	0.5 m
Turbine height (H_t)	0.80 m
Hydrofoil	NACA0018
Number of blades	2
Depth of the turbine centre	2.5 m
Distance from the inlet	$40D_t$
Distance from the outlet	$40D_t$
Undisturbed flow velocity	0.72 m/s

As already described, we are comparing a wind application to our tidal turbine. Therefore, we use the same chord-based Reynolds number to achieve dynamic similarity. Indeed, the lift and drag coefficients used by our turbine model to calculate the forces acting on the blade are strongly Reynolds-dependent, as is the dynamic stall model. However, in the tidal application, the Froude number also has a relevant influence, as mentioned in [27]. The Froude number is given as:

$$F_r = \frac{U_\infty}{\sqrt{g\zeta}} \tag{30}$$

where ζ, as already stated, is the free surface level and thus the dynamic depth of the water column. For example, [28,29] showed how an increase in the Froude number leads to an increase in C_P. Therefore, in our case, it is important to avoid the influence of the Froude number on turbine efficiency. To do this, we use a deep basin (10 m depth) to obtain a rather low F_r (about 0.07). Indeed, when F_r tends to zero, the free surface displacement over the turbine tends to zero, as explained in [29,30], limiting the free surface effects on the turbine.

Figure 3 shows the power coefficients for different TSR values, defined as:

$$C_P = \frac{P}{\frac{1}{2}\rho A_f U_\infty^3} \tag{31}$$

where P is the power generated and A_f is the turbine frontal area. Figure 3 shows several curves relative to different experimental situations and the predictions of the SHYFEM model (blue dots). In particular, there are two sets of data related to the experimental campaign carried out at the GVPM. This is due to the fact that in [25], two identical wind turbines were tested individually. In Figure 3, the triangles represent the *rotor 1* test, and the black squares represent the *rotor 2* test. Due to the small size of the turbine, small manufacturing differences can result in slightly different C_P-TSR curves. However, the two curves are quite similar. No blockage correction is considered for these data series, as the large GVPM test section allows a low blockage ratio (≈1%). Therefore, no blockage corrections need to be applied (blockage corrections are negligible for values below 5%). On the other hand, a correction for the torque losses induced by the drive train is considered. It is determined using the generator as a motor to impose a rotation without a rotor. In this way, the torque sensor measures only a net torque due to friction losses in the drive train. Finally, the yellow triangles represent the data obtained in the OJF and L1-A wind tunnels. In this case, the test section is smaller, and the blockage correction should be applied. However, the data in the figure are those without blockage correction. We can see that the SHYFEM model effectively captures the optimal TSR of 3, and the general trend of the C_P-TSR curve is well reproduced.

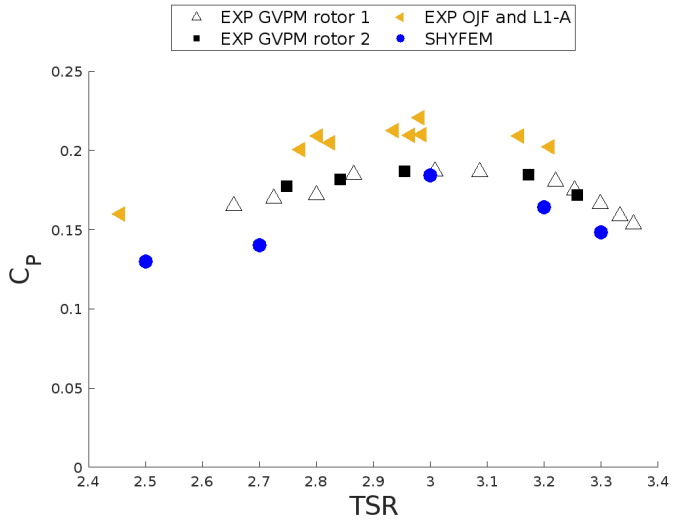

Figure 3. C_P-TSR curves. Comparison between experimental data from GVPM considering two identical rotors (triangles and black squares), the OJF and L1-A wind tunnel experiment (yellow triangles), and the SHYFEM model results (blue dots).

3.2. Wake Validation

For validation of wake development, we consider the same setup as used in the previous section. The simulation time is 21 turbine revolutions, analogous to what was done in [31], where the same experimental situation was studied using high-fidelity CFD simulations. In particular, [31] showed that at least 21 turbine revolutions are required to have a fully developed wake up to 8 diameters downstream of the turbine. All data described below are relative to the optimum TSR, i.e., 3. The comparison is made using the wake development described in [24].

Figure 4 shows the crosswise velocity profiles in the horizontal plane located at the mid-height of the turbine. The experimental measurements are compared with the data obtained using the SHYFEM model, where the simulations are carried out taking into

account the central shaft. The SHYFEM code does not currently allow for the inclusion of solid bodies in the middle of the water column. To account for the shaft effect, we reproduce it by locally cancelling the velocities. This is a very simplified approach, but it allows the effect of the shaft on the surrounding flow field to be reproduced. Therefore, we set all velocity components to zero in the three-dimensional space that the shaft was supposed to occupy. This is the simplest approach for reproducing the shaft effect, and it does not require a tuning process when the case study is changed. A comparison of the SHYFEM prediction with the experimental data shows good agreement in the near wake and the very far wake. The agreement is good in terms of both the velocity deficit and wake thickness.

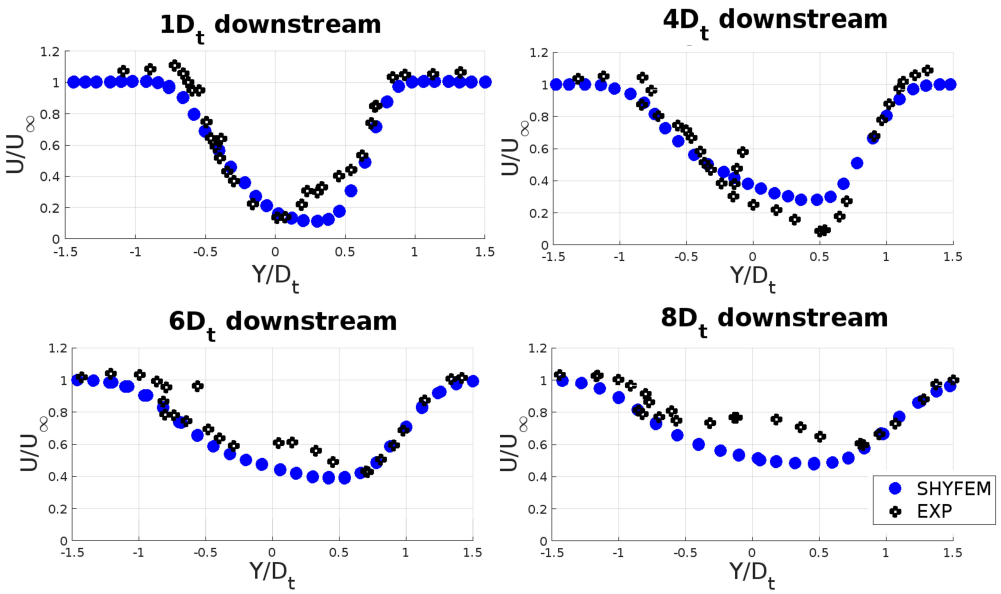

Figure 4. Crosswise velocity profiles at different diameters downstream of the turbine. Comparison between the experimental measurements of Vergaerde et al. [24] and the SHYFEM model including the turbine central shaft.

4. Sensitivity Analysis

For the sensitivity analysis, we use data relative to the wake validation setup. Both the vertical and horizontal resolutions have been modified. Figure 5 shows a comparison of the crosswise velocity profiles relative to the horizontal plane at the mid-height of the turbine. Curves with the same colour represent cases with the same vertical resolution (denoted as "layer" in the figure) in the turbine zone. The green, blue, red, and magenta curves correspond to 0.025 m, 0.05 m, 0.1 m, and 0.15 m resolutions, respectively. Curves with the same symbol refer to the same horizontal grid resolution in the turbine area. Therefore, the symbols used in the legend correspond to specific horizontal resolutions: the dot represents 0.025 m, the diamond represents 0.05 m, the square represents 0.1 m, and the x represents 0.15 m.

The differences in results are most noticeable for the magenta x curve, which has the coarsest grid resolution (0.15 m for both horizontal and vertical). The red curves, with a vertical resolution of 0.1 m, exhibit differences compared to the other data. All the other combinations collapse into a single curve. Therefore, the choice of a grid resolution of 0.05 m for both vertical and horizontal resolutions in the validation task is a good compromise between computational burden and result accuracy. Indeed, there is no relevant difference between the finest case analysed, which is 0.025 m for both vertical and horizontal resolutions.

Table 2 shows the power coefficients obtained for the different cases analysed. As expected, the main differences arise with coarse grids. However, it appears that the power generation is more affected by the horizontal grid resolution than by the vertical layer

thickness. Again, the 0.05 m (i.e., $D_t/10$) horizontal grid resolution seems to be a good compromise between prediction accuracy and computational cost.

Table 2. The power coefficients for the different resolution cases analysed.

C_P	h res [m]	Layer [m]
0.22	0.025	0.05
0.24	0.05	0.05
0.27	0.1	0.05
0.24	0.05	0.025
0.24	0.05	0.1
0.23	0.025	0.025
0.26	0.1	0.1
0.34	0.15	0.15

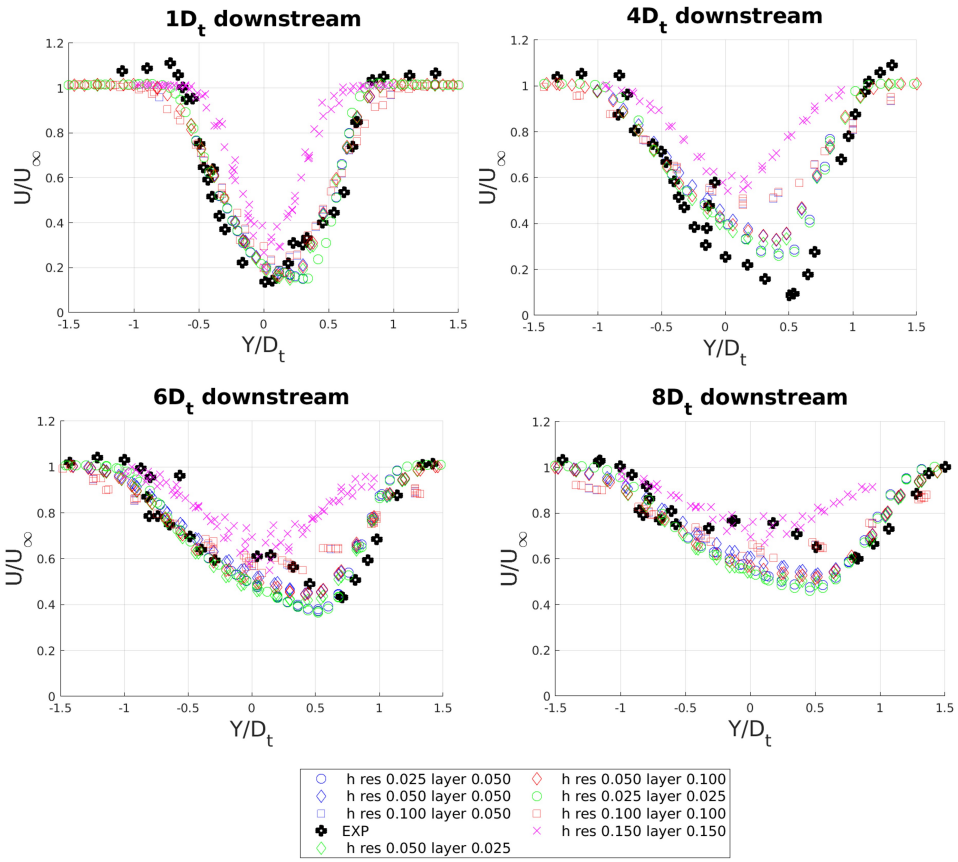

Figure 5. Crosswise velocity profiles on a horizontal plane, located at the mid-height of the turbine, for different grid resolutions.

5. Turbines Interactions

In order to test the SHYFEM code with respect to the turbine interactions, we reproduce the same situation analysed in [32] (blade-resolved CFD simulations), where two pairs of counter-rotating turbines are simulated using the same turbine geometry of the validation task. The case studies are denoted as *A-paired* and *B-paired*, and the direction of turbine rotation is described in Figure 6. The turbines are placed "side by side" with a 1.3 D_t distance between turbine axes. In the results section, the turbines in the orange boxes in Figure 6 are represented. In Figure 7, we qualitatively compare the results obtained in [32] (plots in columns one and three in the figure) with the SHYFEM predictions (plots in columns two and four in the figure). We only aim to make a qualitative comparison of the wakes since [32] used air as the fluid, and therefore the velocities considered were different.

However, the scale of the SHYFEM colour bar (on the right) is such that it reproduces the range of [32]'s colour bar (on the left), scaled by the same factor used to maintain similarity, as explained at the beginning of Section 3. Using wind terminology, the windward and leeward sides of the turbine are considered, as shown at the bottom of the figure. The observer placed upstream of the turbine is considered. In the wake $y - z$ planes, the white rectangle marks the shape of the upper half of the turbine. The black dashed lines in the figure represent the symmetry axes, indicating that on that side is the other turbine of the pair. At first glance, the qualitative agreement between SHYFEM and high-fidelity CFD is good in both situations considered. In the *A-paired* situation, it is clearly visible how the SHYFEM code is able to capture the main features of wake development, particularly the birth of two counter-rotating vortices at the top of the turbine, with a stronger vortex on the windward side, as observed in [32]. The two vortices imply vertical advection, which is beneficial at all distances, and lateral advection, which is always disadvantageous on the windward side. The flow moves from the centre to the outside of the wake, so that the wake on that side appears increasingly larger. The leeward vortex (with an anti-clockwise direction of rotation) tends to bring "fresh flow" from the outside into the wake. However, in the *A-paired* configuration, the other turbine is located on the leeward side, so there is no "fresh flow" to replenish the wake. In the *B-paired* configuration, the dominant vortex on the windward side is located close to the windward side of the other turbine in the pair. This prevents the vortex from widening laterally and consequently expanding vertically. Therefore, despite the hydrostatic nature of the SHYFEM model, it is still possible to reproduce the main features of wake development.

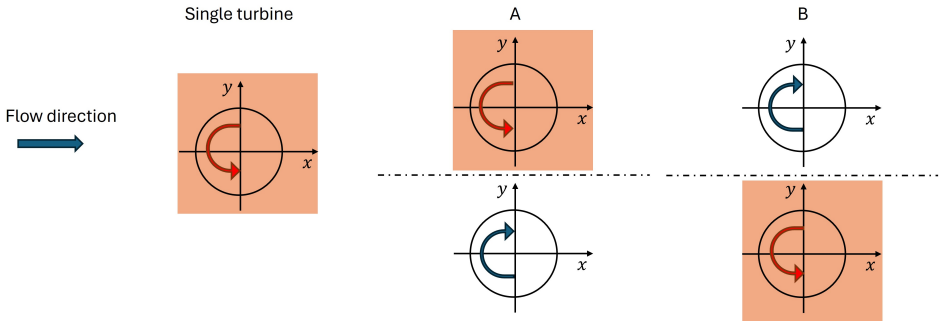

Figure 6. Definition of the direction of rotation for the *A-paired* and *B-paired* case studies.

In terms of performance, [32] found improvements of +7.4% and +2.7% compared to the single turbine for *A-paired* and *B-paired* configurations, respectively. The SHYFEM model achieves a +2% improvement in both situations. In the experiments carried out in [25], the performance gains were about +13% and +15.9% for *A-paired* (inner-downwind in [25]) and *B-paired* (inner-upwind in [25]), respectively. One reason for the poor performance prediction of the SHYFEM model could be its inability to effectively capture the local acceleration around the turbine and within the wake. In particular, in Figure 8, we observe the crosswise dimensionless velocity profile at 1 diameter downstream of the turbine in both the single turbine and paired configurations. Regarding the single turbine, the SHYFEM model shows good agreement with the experimental results in [25] (black dots), while the blade-resolved CFD results (orange dots, relative to the case study described in [32]) show a lower velocity deficit in the near wake due to the absence of the central shaft and a thicker wake compared to both the experimental and SHYFEM model data. Looking at the pairs, in Figure 8, we still observe a lower velocity deficit and a wider wake in the CFD blade-resolved case compared to the SHYFEM model. However, the interesting thing to observe in the case of the paired velocity profile is that the SHYFEM model does not reproduce the local acceleration around the wake, particularly on the side of the channel between the turbines in the pair (left side of the velocity profile). However, the slight increase in power production is likely due to the favourable angle of attack in pair configurations. The power production is affected by both the velocity magnitude and

direction. In the presence of a pair of turbines, the flow is forced to be more rectilinear along the x direction, whereas in a single-turbine configuration, the flow is free to escape laterally from the turbine.

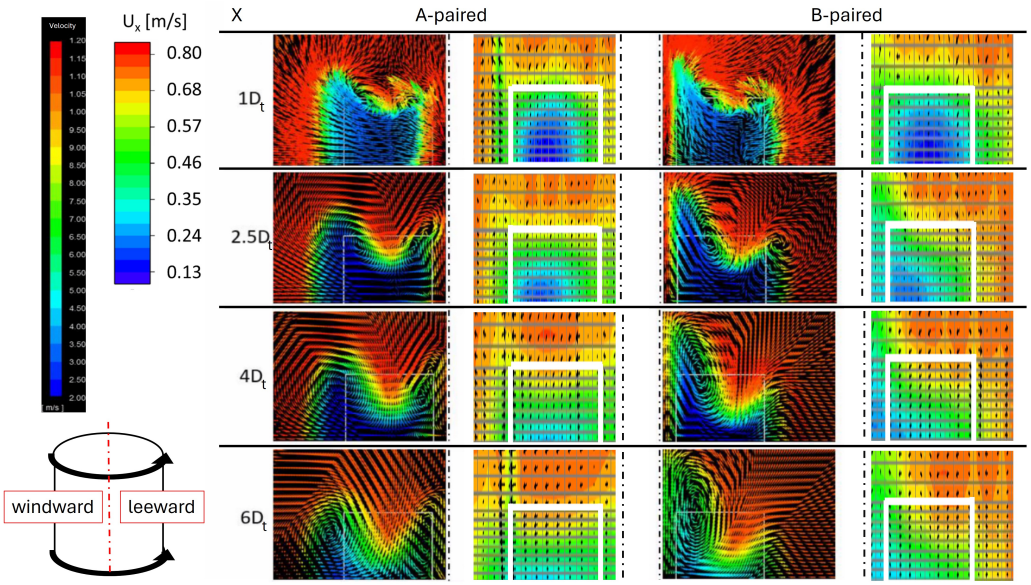

Figure 7. Wake development at 1, 2.5, 4, and 6 diameters downstream of the turbine in a vertical $y - z$ plane. Comparison between Zanforlin et al. [32]'s 2021 results (first and third columns for *A-paired* and *B-paired*, respectively; figures taken from [32]) and the SHYFEM results (second and fourth columns for *A-paired* and *B-paired*, respectively).

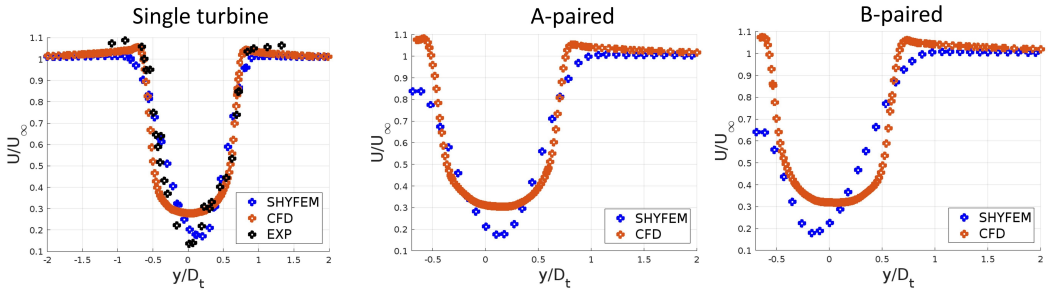

Figure 8. Dimensionless velocity profile at 1 diameter downstream of the turbine. On the left is the single turbine: comparison between experimental data from Vergaerde et al. [25] (black dots), the blade-resolved CFD results from the study in [32] (orange dots), and the SHYFEM model (blue dots). In the centre is the *A-paired* configuration, and on the right is the *B-paired* configuration.

6. Farm Design

In this section, we use our turbine model to simulate farms. To do this, we choose a marine site to deploy our farm and then follow the steps highlighted in Figure 9. First, we need to identify the orientation (θ_{fence}) we want to give our farm, and this is done by evaluating an orientation angle weighted by the power available during flood tide. Then, we need to individualise the spacing between devices in a staggered fence, particularly the lateral and longitudinal spacing (Δx and Δy). To do this, we use fluid dynamic simulations to evaluate the best configuration. Finally, when the fence layout is finalised, we evaluate the influence of several fences on each other by varying the spacing between the fences (ΔX). To optimise the spacing between turbines in a fence and determine the best lateral and longitudinal spacing between devices, fluid dynamic simulations are used. The SHYFEM code is equipped with an automated process that can generate the calculation grid and set up simulations, making this optimisation possible. In this way, it is possible to

simulate a wide range of situations, as already applied in [33] to optimise the spacings for a HATT application.

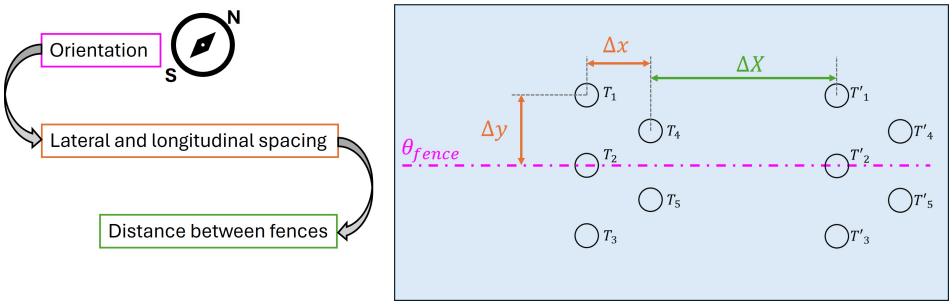

Figure 9. Methodology flowchart.

The method is applied at the Portland Bill marine site as a case study. We characterise the site using the flow data available from Admiralty Chart 2615 (tidal diamond F), as described in [16]. During a flood-ebb tide cycle, the flow directions at this site are widely spread, as shown in Figure 10. This site is chosen in order to analyse a particularly unfavourable situation. By analysing the available power in the tidal current, we can quantify it as proportional to the cube of the undisturbed flow current U as

$$P_{ebb} \propto \sum_{i=1}^{n_{ebb}} U(i)^3 \tag{32}$$

$$P_{flood} \propto \sum_{j=1}^{n_{flood}} U(j)^3 \tag{33}$$

where n_{ebb} and n_{flood} represent the amounts of ebb and flood data, respectively, in the polar graph. During the flood tide, 73% of the total power is available. Therefore, if we want to use turbine fences in this marine area, we have to choose an orientation for the fences. Since most of the power is available during flood tide, we orient the fences to the weighted average direction, calculated as follows:

$$\theta_{fence} = \frac{\sum_{j=i}^{n_{flood}} \theta_{flood}(j) \cdot U(j)^3}{\sum_{j=1}^{n_{flood}} U(j)^3} \approx 242^\circ \tag{34}$$

where θ_{flood} is the azimuth direction of the flood currents shown in Figure 10. In the weighted average, therefore, only the flood tide is taken into account, as it contains most of the available power. So, we consider this orientation for the fences before proceeding with the optimisation analyses.

The turbine considered in this section is the same as the one in the validation task but scaled up 10 times. In this way, we consider a realistic size for farm applications. The full-scale turbine is tested to evaluate the C_P-TSR curve and wake development at higher Reynolds numbers (compared to those of the validation task). The computational domain is $40D_t$ long, $20D_t$ wide, and $10D_t$ deep. The turbine is located $20D_t$ downstream of the inlet and is centred in the domain with respect to the other directions (y and z). The grid resolution in the turbine region is $D_t/10$ (both horizontal and vertical), similar to the results of the sensitivity analysis. Figure 11 shows the C_P-TSR curve for the full-scale turbine compared to the prototype of the validation task. We can see that the C_P curve is higher for the full-scale turbine because it operates at higher Reynolds numbers. The optimal TSR remains almost the same. Since in this section, we are interested in the analysis of tidal farms using the SHYFEM code, we need to be sure that the wake development of the turbine model is well captured at a high Reynolds number. In the experimental study in [34], it was shown that wake development can be considered independent of the Re_D

influence starting from 4×10^5. In our validation task, the Re_D was equal to 3.6×10^5, and by analysing wake development at 1 and 8 diameters downstream of the turbine (Figure 11), we can see negligible differences in wake development by increasing the Reynolds number. Therefore, we can extend the conclusion in [34] to our work. Hence, we can consider the full-scale turbine model validated in terms of wake development and performance for high Reynolds numbers.

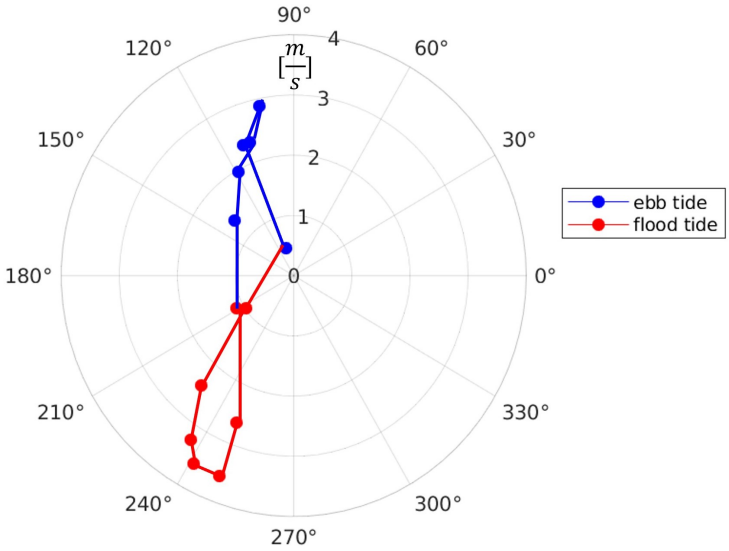

Figure 10. Polar plot relative to the tidal diamond F of Admiralty Chart 2615 (data taken from [16]). The radial direction indicates the magnitude of the velocity in [m/s]. The red dots represent the flood tide, while the blue dots represent the ebb tide.

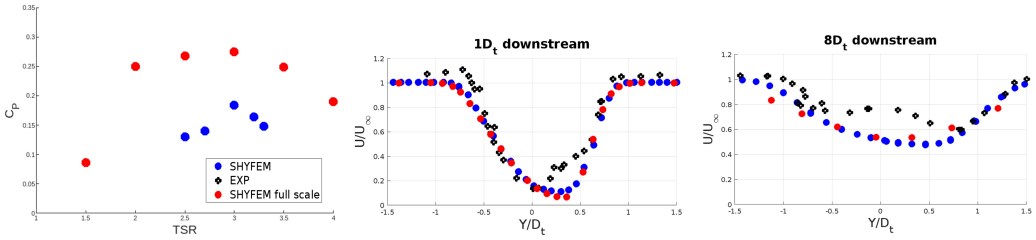

Figure 11. Comparison of the behaviour of a full-scale turbine (red dots) with that of a prototype used for validation (blue dots). The left side shows the C_P-TSR curve, while the right side shows the wake development at 1 and 8 diameters downstream.

6.1. Spacing between Devices in a Fence

As already discussed, we aim to optimise the lateral and longitudinal spacings between turbines in a fence. In particular, we aim to determine the best Δx and Δy distances (based on the chosen marine site), as shown in Figure 12. To this end, we run a series of fluid dynamic simulations (through the automated process), analysing the effect of several $\Delta x - \Delta y$ combinations. The values analysed are summarised in Table 3. To analyse the effect of the distances on the performance of a fence, we must consider a building block of the fence composed of five turbines, as shown in Figure 12. In order to reproduce the effect of the fence, the five turbines must be simulated in a confined area in the horizontal directions. In particular, we must maintain the same distance from the turbines and the lateral boundaries to reproduce the same confinement of the turbines in the fence. In fact, turbines T_1 and T_3 have a distance Δy from the upper and lower lateral boundaries, respectively, to reproduce the lateral confinement of the fence. As already explained in [33], the behaviour of a turbine in a fence is the average between an upstream turbine and a downstream turbine. We consider the behaviour of turbine T_2, which is less affected

by boundary effects and therefore more representative of a turbine in a fence. Turbine T_2 is representative of an upstream turbine when the flow comes from the left ($U_{\infty up}$ in Figure 12), while it represents a downstream turbine when the flow comes from the right ($U_{\infty down}$ in Figure 12). Therefore, to optimise the fence, taking into account the directions of the flood flow (relative to the orientation of the fence), we need to run two simulations for each direction considered, one for each flow direction. In this way, each $\Delta x - \Delta y$ combination is characterised by an averaged power coefficient, defined as follows:

$$C_{P\,av}(j) = \frac{C_{P\,up}(j) + C_{P\,down}(j)}{2} \tag{35}$$

resulting in an averaged performance due to the behaviour of an upstream and a downstream turbine for each j flow direction. These simulations are all performed using an undisturbed flow velocity equal to 1 m/s and the optimal TSR. Therefore, to summarise, refer to Figure 13, which shows the schematic procedure. Each $\Delta x - \Delta y$ combination is tested twice for each j direction of flow. In fact, for a given flow direction, both flow directions must be simulated to obtain the behaviour of an upstream and a downstream turbine within the fence.

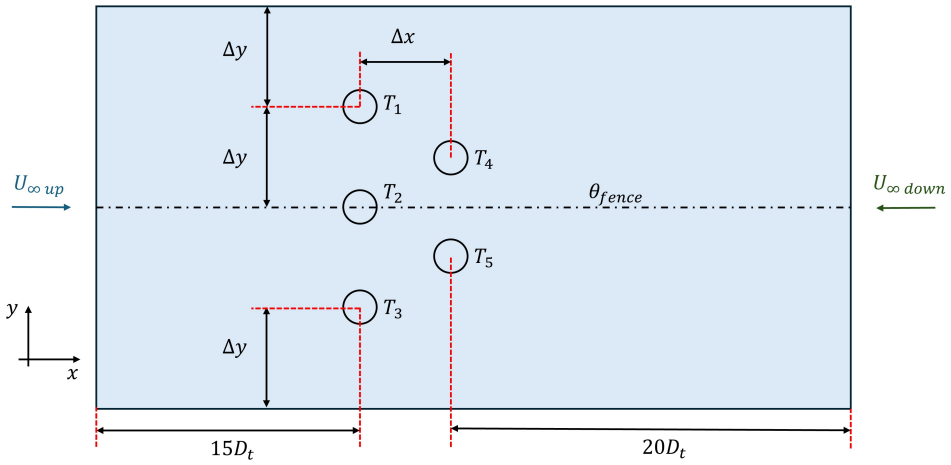

Figure 12. Qualitative top view of the computational domain used to simulate 5 turbines, representative of turbines inside a fence.

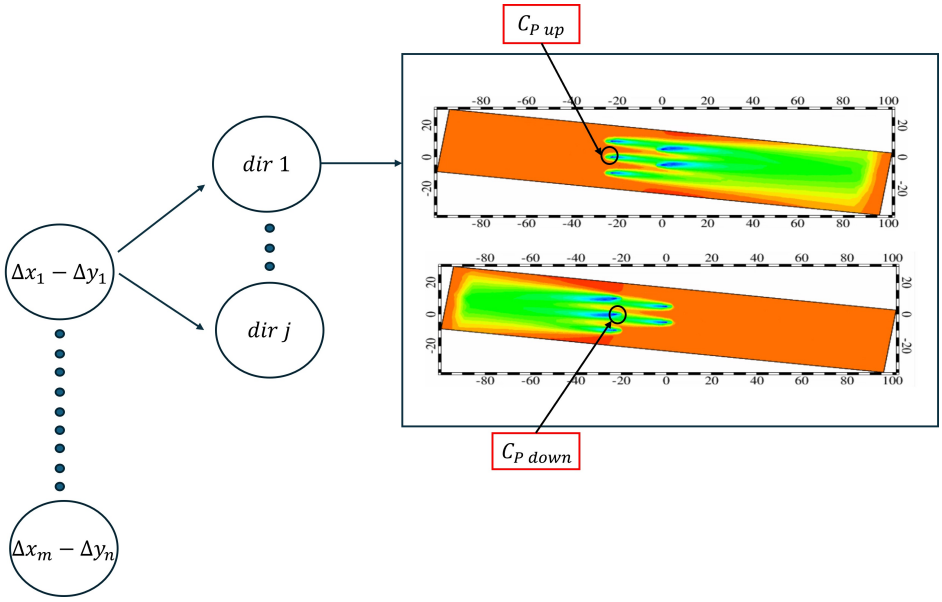

Figure 13. Schematic representation of the optimisation process. Each $\Delta x - \Delta y$ combination is simulated twice for each j flow direction using both flow directions to obtain $C_{P\,up}$ and $C_{P\,down}$.

Then, to calculate the behaviour of the fence, taking into consideration all of the flow directions, we make a weighted average as follows:

$$\overline{C}_P = \frac{\sum_{j=1}^{n_{flood}} C_{P\,av}(j) \cdot U(j)^3}{\sum_{j=1}^{n_{flood}} U(j)^3} \tag{36}$$

and in this way, we evaluate the best layout by weighting with the available power content.

Some might ask why use five turbines as a fence block instead of three. This choice makes it possible to evaluate the behaviour of the fence in several flow conditions. Indeed, when considering only three turbines in several $\Delta x - \Delta y$ combinations, especially with high values of Δx, it may happen that for certain θ_{flood} and certain Δx values, one of the three turbines remains outside the calculation domain. This happens because in the SHYFEM code, we keep the fence orientation fixed (θ_{fence}) while we "rotate" the external domain to ensure an inlet/outlet flow always perpendicular to the inlet/outlet boundaries. It is not really a rotation since we keep the width of the domain (along the y direction) always equal to $4\Delta y$ to reproduce the fence confinement for each flow direction.

Thus, to analyse all the combinations listed in Table 3, 160 simulations are required. Each combination must be tested twice (in both directions) for each of the five flood directions (we neglected only one value lower than 1 m/s). As already explained, it is possible to carry out such a large number of simulations thanks to the automated process developed for the SHYFEM code (already used for HATTs in [33]). The best result is achieved with the combination $\Delta x = 2D_t$ and $\Delta y = 3D_t$, which yields $\overline{C}_P = 0.301$. These lateral and longitudinal spacings are chosen to build the whole fence.

Table 3. Combinations of $\Delta x - \Delta y$ analysed through fluid dynamic simulations. $\overline{C}_P$ represents the performance of a turbine within the fence.

Δy	Δx	$\overline{C}_P$
$2D_t$	$2D_t$	0.280
	$3D_t$	0.262
	$4.5D_t$	0.242
	$7D_t$	0.231
$3D_t$	$2D_t$	0.301
	$3D_t$	0.298
	$4.5D_t$	0.284
	$7D_t$	0.257
$4.5D_t$	$2D_t$	0.300
	$3D_t$	0.299
	$4.5D_t$	0.296
	$7D_t$	0.284
$7D_t$	$2D_t$	0.296
	$3D_t$	0.295
	$4.5D_t$	0.293
	$7D_t$	0.292

6.2. Spacing between Fences

We now place three fences, each consisting of seven turbines, and analyse the effect of the distance between the fences, i.e., the ΔX described in Figure 14. The turbine adopted is the same as the one in Section 6.1, and all settings, if not explicitly specified, are the same as those in Section 6.1. The computational domain extends $20D_t$ from the farm in each direction (north, south, east, and west), as shown in Figure 14. These dimensions are sufficient to avoid relevant blockage effects, as already observed in a similar sensitivity analysis regarding proximity to the boundary, carried out in [35].

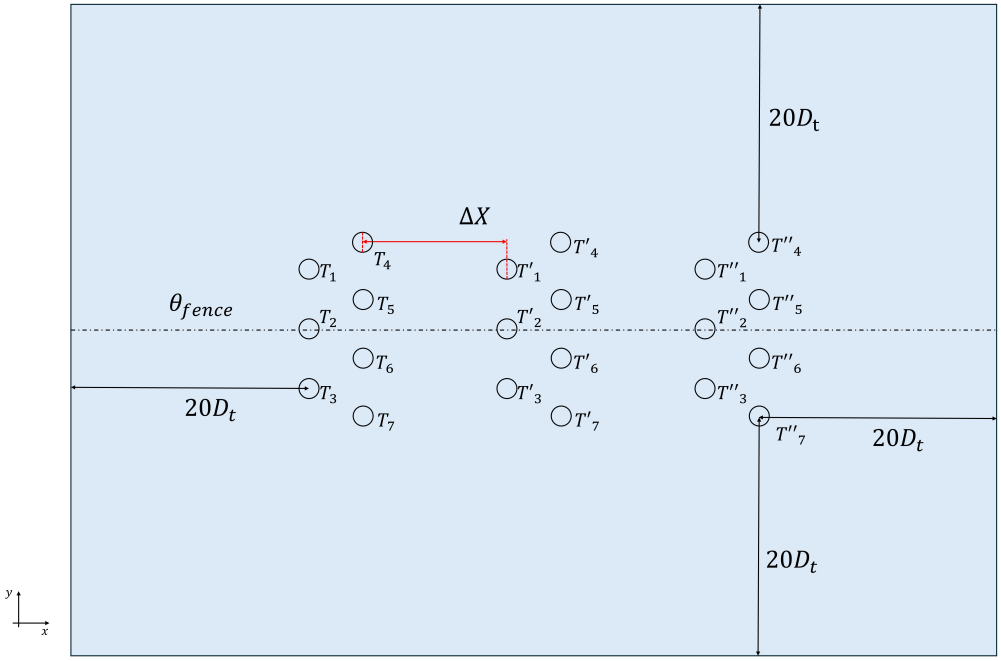

Figure 14. Qualitative top view of the calculation domain used for the farm application.

The ΔX values chosen are $2D_t$, $4D_t$, $6D_t$, and $8D_t$. The three fences are tested for all the flow conditions occurring at Portland Bill (both flood and ebb) using the velocities shown in Figure 10 as the undisturbed flow velocity.

7. Results

In Figure 15a, we highlight the average C_P of the whole farm, obtained as the arithmetic mean of the C_P of each turbine in the farm. It can be clearly seen that the performance of the farm is hardly affected by the change in ΔX during the flood tide (red bubble). On the other hand, the effect of ΔX is clearly visible during ebb tide (blue bubble). In particular, the greater the ΔX, the better the performance of the farm. This beneficial effect is not as relevant during the flood tide because even if the farm is enlarged, the same number of devices will be in the wake of the others. However, during the ebb tide, due to the skewed currents, the change in ΔX frees some devices from the wakes of other turbines. This can be clearly seen in Figure 16, where a flood tide stream (top) and an ebb tide stream (bottom) are compared for different ΔX values ($2D_t$ on the left and $8D_t$ on the right). At first glance, it is evident that the ebb tide is favoured by wider fence spacing. Furthermore, the average C_P shown in Figure 15 also shows this trend. In fact, the average C_P during the flood tide is generally lower than the average C_P during the ebb tide, which means that more turbines are in the wake during the flood tide.

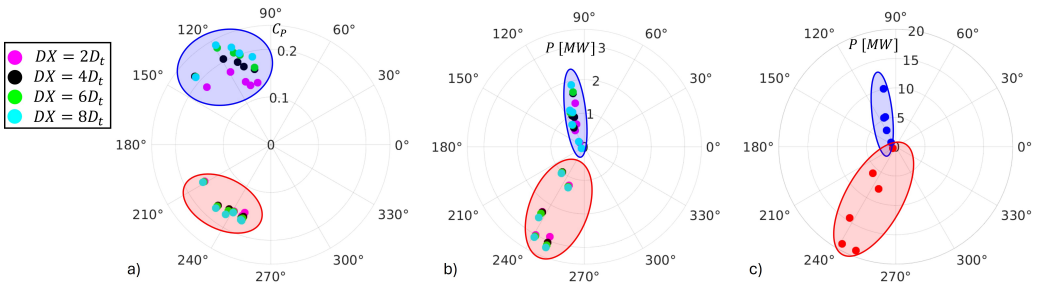

Figure 15. (**a**) The average C_P of the farm; (**b**) the power generated by the whole farm; and (**c**) the power available in the current. The red and blue bubbles represent the flood and ebb tides, respectively.

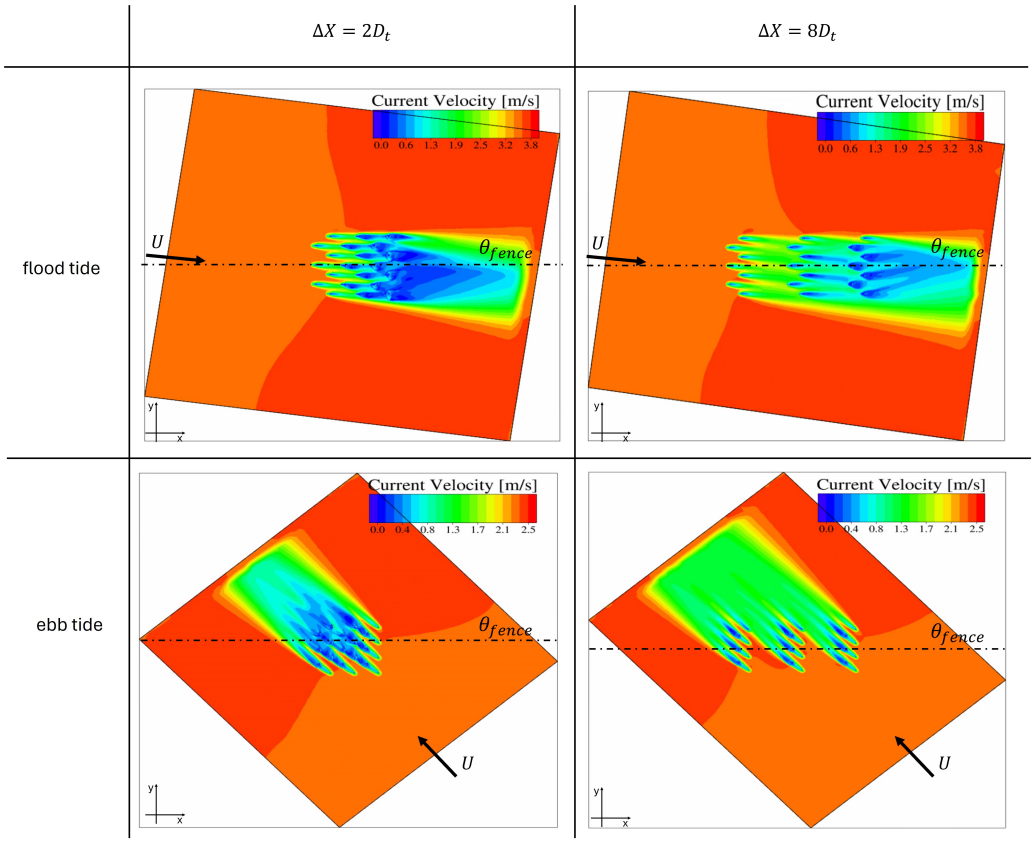

Figure 16. Flow field of a flood and ebb tide current, top and bottom, respectively, for different ΔX values ($2D_t$ on the left and $8D_t$ on the right).

The global power generated by the farm (as the sum of the farm power for each flow direction) increases by +16% moving from $\Delta X = 2D_t$ to $8D_t$. At the same time, the sea area A_h covered by the farm, i.e., the horizontal encumbrance, increases by 2.2 times (the area covered by the farm is a rectangle with edges l_1 and l_2, where $l_1 = 3 \cdot \Delta y$ and $l_2 = 3 \cdot \Delta x + 2 \cdot \Delta X$). Even though there is a slight increase in performance when increasing the value of ΔX, it is mainly noticeable during ebb tide. But, ebb tide has a lower power content (approximately 27% of the total), so the increase in performance is not as relevant from the point of view of power generation. In fact, if we compare Figure 15b,c (generated power and available power, respectively), we can see that the trend in power generation is mainly influenced by the available power. Therefore, the small increase in power does not justify such an expansion of the exploited sea area, as it may conflict with other stakeholders' interests. It is more reasonable to achieve the same power production as the $\Delta X = 8D_t$ configuration by adding a few devices to the $\Delta X = 2D_t$ configuration.

In this study, we analysed the effect of the distance between turbine fences for a particularly unfavourable site. Indeed, Portland Bill is well suited as a marine site in terms of the magnitude of the velocities occurring, but it shows a wide spread in flow directions. There are other marine sites characterised by a more regular flow reversal during a tidal cycle, with a flow reversal of almost 180°. Some examples are the Fromveur Strait in western Brittany [36], the Pentland Firth in Scotland [37], and Almwch, Bardsey Sound, and Ramsey Sound in Wales UK [38]. If we imagine placing our farm with three fences in such a marine site, we would probably detect an even smaller increase in power generation by increasing ΔX. In fact, the same situation that characterised the flood tide, i.e., ΔX does not influence the number of devices in the wake of others, would also characterise the ebb tide, thus losing the advantages seen in this case study. In fact, in a more regular and almost mirror-like situation between the flood and ebb tides, the same observations of the flood tide can be applied to the ebb tide. Therefore, in a more regular marine site, the

benefit of increasing ΔX would be even less significant, and this would certainly not justify increasing the horizontal size of the farm.

8. Conclusions

This paper presents the development, validation, and application of a 3D BEM model of a vertical-axis tidal turbine. The model was embedded in the shallow-water code SHYFEM using a momentum sink approach. We have shown the ability of this model to predict the behaviour of the turbine in terms of power generation and wake development. The simplicity of the model enables fast computation, but the blade-element approach ensures accurate reproduction of a specific turbine, taking into account the geometric design and the operating conditions (chord, blade pitch, TSR, etc.).

The novelty of this work lies in the fact that to the best of the authors' knowledge, it is the first time that a model for vertical-axis tidal turbines has been included in a regional code. Furthermore, the model is based on BEM theory, enabling accurate environmental and energy studies. By coupling the structure of the code (shallow-water equations) with the BEM approach of the turbine model, the tool proves to be particularly suitable for cluster/farm studies. Indeed, it allows for fast computation time with accurate results. As an application, in this paper, the model was used to design a tidal farm. In particular, 160 fluid dynamic simulations were used to determine the best spacing between turbines in a fence. This large number of simulations was carried out using an automated process developed for the SHYFEM code. Once the best spacing for the fence was determined, we analysed a farm consisting of three fences. In particular, we analysed the effect of the distance between the fences.

What emerged was that most of the advantages of distancing the fences occurred at ebb tide, characterised by a lower power content. We observed an increase of 16% in the generated power, and at the same time, a relevant increase in the horizontal marine area occupied by the farm. These results were obtained for a marine site located at Portland Bill, characterised by a wide spread of flow direction during a tidal cycle. It is reasonable to conclude that for other marine sites characterised by a more regular inversion of flow during a tidal cycle (almost 180°), the benefits in terms of power generation would be even lower. So, in general, increasing the spacing between the fences of turbines cannot be considered a valid technique to increase the power generation of a farm. Indeed, the same power output of the farm obtained with $\Delta X = 8D_t$ can be achieved with $\Delta X = 2D_t$ by adding a few devices, for example. This would allow for the limitation of the horizontal sea area used for energy purposes in order to account for other possible stakeholders interested in the same area.

Future developments of this work may involve using the automated process developed for the SHYFEM code to optimise the farm layout for VATTs by investigating other farm configurations, abandoning the fence concept, and hopefully carrying out simulation-based optimisations.

Author Contributions: Conceptualisation, M.P. and S.Z.; methodology, M.P. and S.Z.; software, M.P. and R.S.; validation, M.P.; data curation, M.P. and R.S.; writing—original draft preparation, M.P.; writing—review and editing, M.P.; supervision, M.P. and S.Z. All authors have read and agreed to the published version of the manuscript.

Funding: This research was funded by the National Recovery and Resilience Plan (NRRP), CN1, Centro Nazionale di Ricerca in High-Performance Computing, Big Data e Quantum Computing, spoke 6: multiscale modelling and engineering applications.

Data Availability Statement: The raw data supporting the conclusions of this article will be made available by the authors on request.

Conflicts of Interest: The authors declare no conflicts of interest.

References

1. Zhang, C.; Kramer, S.C.; Angeloudis, A.; Zhang, J.; Lin, X.; Piggott, M.D. Improving tidal turbine array performance through the optimisation of layout and yaw angles. *Int. Mar. Energy J.* **2022**, *5*, 273–280. [CrossRef]
2. Funke, S.W.; Kramer, S.C.; Piggott, M.D. Design optimisation and resource assessment for tidal-stream renewable energy farms using a new continuous turbine approach. *Renew. Energy* **2016**, *99*, 1046–1061. [CrossRef]
3. García-Oliva, M.; Djordjević, S.; Tabor, G.R. The impacts of tidal turbines on water levels in a shallow estuary. *Int. J. Mar. Energy* **2017**, *19*, 177–197. [CrossRef]
4. Brown, A.J.G.; Neill, S.P.; Lewis, M.J. Tidal energy extraction in three-dimensional ocean models. *Renew. Energy* **2017**, *114*, 244–257. [CrossRef]
5. Robins, P.E.; Neill, S.P.; Lewis, M.J. Impact of tidal-stream arrays in relation to the natural variability of sedimentary processes. *Renew. Energy* **2014**, *72*, 311–321. [CrossRef]
6. De Dominicis, M.; Murray, R.O.; Wolf, J. Multi-scale ocean response to a large tidal stream turbine array. *Renew. Energy* **2017**, *114*, 1160–1179. [CrossRef]
7. Deng, G.; Zhang, Z.; Li, Y.; Liu, H.; Xu, W.; Pan, Y. Prospective of development of large-scale tidal current turbine array: An example numerical investigation of Zhejiang, China. *Appl. Energy* **2020**, *264*, 114621. [CrossRef]
8. Ramos, V.; Carballo, R.; Sanchez, M.; Veigas, M.; Iglesias, G. Tidal stream energy impacts on estuarine circulation. *Energy Convers. Manag.* **2014**, *80*, 137–149. [CrossRef]
9. Ramos, V.; Carballo, R.; Ringwood, J.V. Application of the actuator disc theory of Delft3D-FLOW to model far-field hydrodynamic impacts of tidal turbines. *Renew. Energy* **2019**, *139*, 1320–1335. [CrossRef]
10. Thiébot, J.; Guillou, S.; Nguyen, V.T. Modelling the effect of large arrays of tidal turbines with depth-averaged Actuator Disks. *Ocean Eng.* **2016**, *126*, 265–275. [CrossRef]
11. Roc, T.; Conley, D.C.; Greaves, D. Methodology for tidal turbine representation in ocean circulation model. *Renew. Energy* **2013**, *51*, 448–464. [CrossRef]
12. Lin, J.; Sun, J.; Liu, L.; Chen, Y.; Lin, B. Refined representation of turbines using a 3D SWE model for predicting distributions of velocity deficit and tidal energy density. *Int. J. Energy Res.* **2015**, *39*, 1828–1842. [CrossRef]
13. Pucci, M.; Di Garbo, C.; Bellafiore, D.; Zanforlin, S.; Umgiesser, G. A BEM-Based Model of a Horizontal Axis Tidal Turbine in the 3D Shallow Water Code SHYFEM. *J. Mar. Sci. Eng.* **2022**, *10*, 1864. [CrossRef]
14. SHYFEM-Model. Available online: https://github.com/SHYFEM-model/shyfem (accessed on 6 March 2024).
15. Ouro, P.; Stoesser, T. An immersed boundary-based large-eddy simulation approach to predict the performance of vertical axis tidal turbines. *Comput. Fluids* **2017**, *152*, 74–87. [CrossRef]
16. Zanforlin, S. Advantages of vertical axis tidal turbines set in close proximity: A comparative CFD investigation in the English Channel. *Ocean Eng.* **2018**, *156*, 358–372. [CrossRef]
17. Zheng, H.D.; Zheng, X.; Zhao, S. Arrangement of clustered straight-bladed wind turbines. *Energy* **2020**, *200*, 117563. [CrossRef]
18. Sun, K.; Ji, R.; Zhang, J.; Li, Y.; Wang, B. Investigations on the hydrodynamic interference of the multi-rotor vertical axis tidal current turbine. *Renew. Energy* **2021**, *169*, 752–764. [CrossRef]
19. Shamsoddin, S.; Porté-Agel, F. A large-eddy simulation study of vertical axis wind turbine wakes in the atmospheric boundary layer. *Energies* **2016**, *9*, 366. [CrossRef]
20. Ouro, P.; Dené, P.; Garcia-Novo, P.; Stallard, T.; Kyozuda, Y.; Stansby, P. Power density capacity of tidal stream turbine arrays with horizontal and vertical axis turbines. *J. Ocean Eng. Mar. Energy* **2023**, *9*, 203–218. [CrossRef]
21. Jégo, L.; Guillou, S.S. Study of a bi-vertical axis turbines farm using the actuator cylinder method. *Energies* **2021**, *14*, 5199. [CrossRef]
22. Rocchio, B.; Chicchiero, C.; Salvetti, M.V.; Zanforlin, S. A simple model for deep dynamic stall conditions. *Wind Energy* **2020**, *23*, 915–938. [CrossRef]
23. Migliore, P.; Wolfe, W.; Fanucci, J. Flow curvature effects on Darrieus turbine blade aerodynamics. *J. Energy* **1980**, *4*, 49–55. [CrossRef]
24. Vergaerde, A.; De Troyer, T.; Muggiasca, S.; Bayati, I.; Belloli, M.; Kluczewska-Bordier, J.; Parneix, N.; Silvert, F.; Runacres, M.C. Experimental characterisation of the wake behind paired vertical-axis wind turbines. *J. Wind. Eng. Ind. Aerodyn.* **2020**, *206*, 104353. [CrossRef]
25. Vergaerde, A.; De Troyer, T.; Standaert, L.; Kluczewska-Bordier, J.; Pitance, D.; Immas, A.; Silvert, F.; Runacres, M.C. Experimental validation of the power enhancement of a pair of vertical-axis wind turbines. *Renew. Energy* **2020**, *146*, 181–187. [CrossRef]
26. Brusca, S.; Lanzafame, R.; Messina, M. Flow similitude laws applied to wind turbines through blade element momentum theory numerical codes. *Int. J. Energy Environ. Eng.* **2014**, *5*, 313–322. [CrossRef]
27. Jump, E.; Macleod, A.; Wills, T. Review of tidal turbine wake modelling methods: State of the art. *Int. Mar. Energy J.* **2020**, *3*, 91–100. [CrossRef]
28. Hunt, A.; Stringer, C.; Polagye, B. Effect of aspect ratio on cross-flow turbine performance. *J. Renew. Sustain. Energy* **2020**, *12*, 054501. [CrossRef]
29. Vogel, C.; Houlsby, G.; Willden, R. Effect of free surface deformation on the extractable power of a finite width turbine array. *Renew. Energy* **2016**, *88*, 317–324. [CrossRef]

30. Whelan, J.I.; Graham, J.; Peiro, J. A free-surface and blockage correction for tidal turbines. *J. Fluid Mech.* **2009**, *624*, 281–291. [CrossRef]
31. Zanforlin, S. Effects of hydrofoil shape and turbine solidity on the wake energy recovery in cross-flow turbines. *J. Ocean Eng. Mar. Energy* **2023**, *9*, 547–566. [CrossRef]
32. Zanforlin, S.; Lupi, P. Investigation of the wake energy recovery of cross-flow turbines in paired configuration by means of 3d-CFD and analysis of the streamwise momentum budget. In Proceedings of the 76th Italian National Congress ATI (ATI 2021), Rome, Italy, 15–17 September 2021; E3S Web of Conferences; Volume 312, p. 08011.
33. Pucci, M.; Zanfrolin, S. Tidal Farms: Optimising site-specific layouts by combining analytical methods and fluid dynamic simulations. In Proceedings of the International Conference on Artificial Intelligence, Computer, Data Sciences and Applications (ACDSA 2024), Victoria, Seychelles, 1–2 February 2024; pp. 463–468.
34. Bachant, P.; Wosnik, M. Reynolds number dependence of cross-flow turbine performance and near-wake characteristics. In Proceedings of the 2nd Marine Energy Technology Symposium, Seattle, WA, USA, 15–18 April 2014.
35. Pucci, M.; Bellafiore, D.; Zanforlin, S.; Frangioni, A. A turbines-module adapted to the marine site for tidal farms layout optimization. In Proceedings of the European Wave and Tidal Energy Conference, Bilbao, Spain, 3–7 September 2023; Volume 15.
36. El Tawil, T.; Guillou, N.; Charpentier, J.F.; Benbouzid, M. On tidal current velocity vector time series prediction: A comparative study for a French high tidal energy potential site. *J. Mar. Sci. Eng.* **2019**, *7*, 46. [CrossRef]
37. Lande-Sudall, D.; Stallard, T.; Stansby, P. Co-located offshore wind and tidal stream turbines: Assessment of energy yield and loading. *Renew. Energy* **2018**, *118*, 627–643. [CrossRef]
38. Piano, M.; Neill, S.; Lewis, M.; Robins, P.; Hashemi, M.R.; Davies, A.; Ward, S.; Roberts, M. Tidal stream resource assessment uncertainty due to flow asymmetry and turbine yaw misalignment. *Renew. Energy* **2017**, *114*, 1363–1375. [CrossRef]